Chapter 1

Quantum Image-Forming Theory for Calculation of Resolution Limit in Laser Microscopy

Naoki Fukutake

Additional information is available at the end of the chapter

http://dx.doi.org/ 10.5772/63494

Abstract

Here we show what determines the optical resolution in laser microscopy. We define the expanded resolution limit (spatial frequency cutoff) that includes the classic Abbe definition as 2 NA/λ, where λ is the wavelength. The resolution limit can approximately be redefined as the frequency cutoff αNA/λ, where α is the constant that depends on the optical process occurring in the sample. In the case of the optical process originating from the linear susceptibility $\chi^{(1)}$, the resolution limit is well known as the Abbe definition, namely, $\alpha = 2$. However, when other optical processes are harnessed to form the image through laser microscopy, the resolution limit can differ. We formulate a theoretical framework that can calculate the expanded resolution limits of all kinds of laser microscopy utilizing coherent, incoherent, linear, and nonlinear optical processes.

Keywords: image-forming theory, nonlinear optical microscopy, optical transfer function, optical resolution limit, light-matter interaction

1. Introduction

The resolution limit (spatial frequency cutoff) of optical microscopy is usually described as 2 NA/λ, where λ is the wavelength [1]. For example, bright field microscopy indicates the resolution limit of 2 NA/λ at a maximum. However, this resolution limit is restricted to optical microscopy that utilizes the optical process derived from the linear susceptibility $\chi^{(1)}$, such as bright field microscopy. Since fluorescence is a $\chi^{(3)}$-derived optical process, the resolution limit of optical microscopy with fluorescence can differ from that of bright field microscopy. Although conventional fluorescence microscopy exhibits the resolution limit of 2 NA/λ, microscopy that achieves the full potential of fluorescence, such as structured illumination

microscopy (SIM), can reach 4 NA/λ [2]. In general, the resolution limit in optical microscopy becomes different according to the kind of optical process.

Laser microscopy is composed of an excitation optical system and a signal-collection optical system, and the signals are acquired point by point to reconstruct an image. One of the typical examples of laser microscopy is confocal fluorescence microscopy, which has been widely used as an optical imaging technique. Confocal fluorescence microscopy can acquire high-resolution optical images with depth sectioning by means of focused laser excitation and a pinhole in front of a detector, which eliminates out-of-focus signals. Confocal fluorescence microscopy harnesses fluorescence as an optical process to increase the optical resolution, compared with microscopy with a $\chi^{(1)}$-derived optical process. Confocal microscopy that utilizes a $\chi^{(1)}$-derived optical process has a resolution limit (frequency cutoff) of $NA_{ex}/\lambda_{ex} + NA_{col}/\lambda_{ex}$, where λ_{ex} is the wavelength of the excitation beam, NA_{ex} is the numerical aperture of the objective in the excitation system, and NA_{col} is the numerical aperture of the objective in the signal-collection system [3, 4], while confocal fluorescence microscopy theoretically indicates the resolution limit of $2NA_{ex}/\lambda_{ex} + 2\ NA_{col}/\lambda_{fl}$, where λ_{fl} is the wavelength of the fluorescence. Note that in conventional (wide field) fluorescence microscopy, since the entire specimen is excited evenly, which corresponds to the condition $NA_{ex} = 0$, the resolution limit becomes $2\ NA_{col}/\lambda_{fl}$.

In addition to confocal fluorescence microscopy, various laser microscopy techniques have recently been used to visualize biological specimens in three dimensions by harnessing many kinds of optical processes, such as two-photon excited fluorescence (TPEF), second-order harmonic generation (SHG), third-order harmonic generation (THG), coherent anti-Stokes Raman scattering (CARS), and stimulated Raman scattering (SRS) [5–11]. Depending on the optical process, each microscopy exhibits its own feature of image formation. In incoherent optical processes, such as fluorescence and TPEF, since the vacuum field is involved in the phenomena along with the excitation beam, the signals emitted from different molecules in the specimen do not interfere. In contrast, in coherent optical processes, such as $\chi^{(1)}$-derived phenomenon, SHG, THG, CARS, and SRS, because the processes are caused only by coherent excitation laser beams, the signals emitted from different molecules interfere. Although the coherence of the optical process influences the image-forming properties of laser microscopy, the basic concept is that the image of the linear or nonlinear susceptibility distribution $\chi^{(i)}(x, y, z)$ in the specimen is formed by microscopy regardless of coherence. From a perspective other than coherence, laser microscopy can be categorized into two types. In the first type, as the wavelength of the signal is different from that of the excitation beam, the signal can be separated from the excitation beam, resulting in the image being formed only by the signal. In the second type, since the signal has the same wavelength as the excitation beam, interference between the signal and the excitation beam is observed. It will be shown that the image-forming properties and resolution limits of both types can be dealt with in the identical framework.

Although the image-forming properties of each microscopy technique are well known, the unified theory does not exist that can deal with the image-forming properties and the resolution limits of all kinds of laser microscopy in the identical framework. If the unified image-forming theory is developed, it enables one to overview all microscopy techniques with any

http://dx.doi.org/ 10.5772/63494

optical processes, such as linear, nonlinear, coherent, and incoherent processes, which can lead to the invention of a new microscopy technique. In this chapter, we formulate a unified framework that utilizes double-sided Feynman diagrams to discuss all microscopy applications by use of a unique technique. With our framework, the resolution limits of laser microscopy techniques will be able to be redefined with respect to each optical process. Moreover, we will lead to some important conclusions about laser microscopy. Although only laser microscopy is discussed here, our theory can be applied to any type of optical microscopy.

2. Theoretical framework

2.1. Model description

We begin by defining the imaging system (laser microscopy) in our model. Laser microscopy is composed of an excitation system to focus the laser beam onto a sample and a signal-collection system to gather the signal generated from the sample. A schematic of laser microscopy is shown in **Figure 1**, in which the coordinate systems are given. We assume in what follows that three-dimensional (3-D) sample-stage scanning is conducted instead of laser scanning, but it does not influence the optical resolution. In laser microscopy, usually one or two excitation beams are employed to generate the signal. The electric field of the signal is emitted from the molecule excited by the electric fields of excitation beams, and the signal field propagates through the signal-collection system. The signals are acquired point by point with a photodetector to reconstruct the 3-D image.

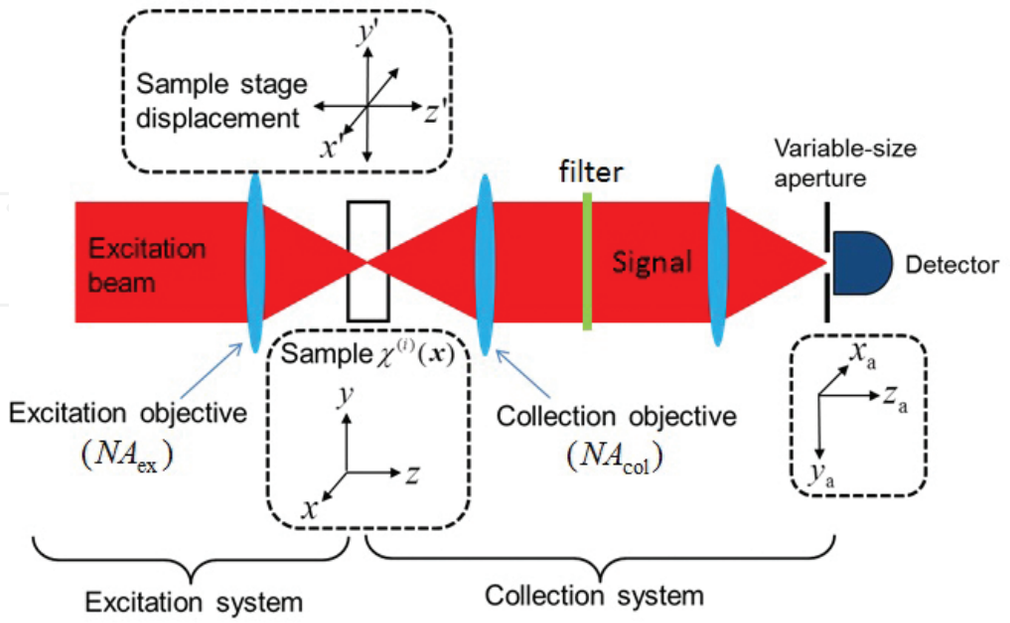

Figure 1. Schematic of laser microscopy (transmission type).

For simplicity, the first Born approximation is applied to understand the true nature of the optical resolution. In this approximation, the multiple scattering and depletion of the beam are neglected, which usually holds true for nearly transparent samples, such as a biological specimen. If the multiple scattering and depletion were intense, the image acquired would become deformed to some degree. We assume that both the excitation and signal-collection systems are 1× magnification systems with no aberration, which does not change the essence of their image-forming properties. In our model, the scalar diffraction theory is employed. The linear or nonlinear susceptibility distribution $\chi^{(i)}(x, y, z)$ in the sample plays a role as the object in the imaging system. The polarization $P(x, y, z)$ is induced by the excitation electric field, and the induced polarization emits the signal electric field. Hereafter, we express the electric field as a complex function.

2.2. Transmission linear confocal microscopy

We start with transmission linear confocal microscopy, in which a $\chi^{(1)}$-derived optical process occurs in the sample. **Figure 2** shows the double-sided Feynman diagram and the energy-level diagram describing the$\chi^{(1)}$-derived optical process. The polarization is induced by the excitation beam focused onto the sample, and the signal emitted by the polarization is gathered and delivered into the photodetector through the signal-collection system. We express the electric field distribution in the sample formed by the focused excitation beam as $E_{ex}(x, y, z)$. The Fourier transform of $E_{ex}(x, y, z)$ is shaped like a portion of a spherical shell, as shown in **Figure 3**, which represents the distribution of the wavenumber vector. When the sample-stage displacement (x', y', z') is zero, the polarization distribution becomes

$$P(x, y, z) = \chi^{(1)}(x, y, z) E_{ex}(x, y, z), \tag{1}$$

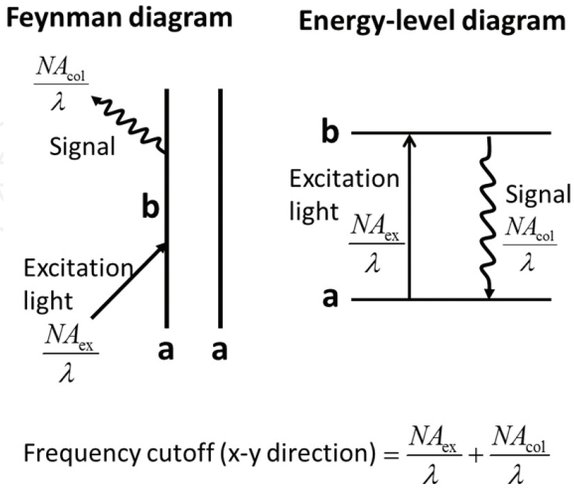

Figure 2. Double-sided Feynman diagram and energy-level diagram for the $\chi^{(1)}$-derived optical process. λ is the wavelength. The frequency cutoff (x-y direction) can be calculated by using the diagrams, which will be discussed in more detail in a later section.

http://dx.doi.org/ 10.5772/63494

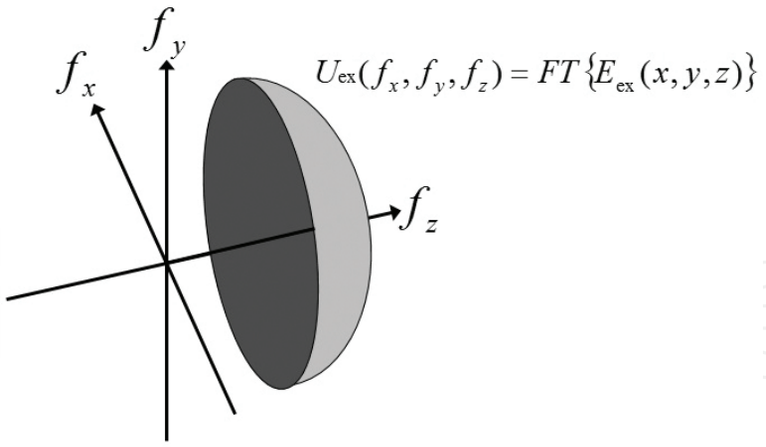

Figure 3. Distribution of the wavenumber vector for the beam focused by the objective. This is referred to as the "3-D pupil function".

where $\chi^{(1)}(x, y, z)$ is the linear susceptibility distribution in the sample and we presume that the electric permittivity $\in_0$ of free space is unity: $\in_0 = 1$. We assume that the signal emitted from a single point in the sample located at the origin ($(x, y, z) = (0, 0, 0)$) of the object coordinate forms the electric field distribution $E_{col}(x_a, y_a, z_a)$ in the detection space through the signal-collection system. The Fourier transform of $E_{col}(x_a, y_a, z_a)$ is also shaped like a portion of a spherical shell located on the $+k_z$ side. Using $E_{col}(x_a, y_a, z_a)$ and $P(x, y, z)$, the electric field distribution $E_T(x_a, y_a, z_a)$ in the detection space in the case of arbitrary $\chi^{(1)}(x, y, z)$ is given by

$$E_T(x_a, y_a, z_a) = \iiint P(x, y, z) E_{col}(x_a - x, y_a - y, z_a - z) dx dy dz, \tag{2}$$

when $(x', y', z') = (0, 0, 0)$. Taking into account the sample-stage displacement (x', y', z'), we recast Eq. (2) as

$$\begin{aligned} &E_T(x', y', z'; x_a, y_a, z_a) \\ &= \iiint \chi^{(1)}(x + x', y + y', z + z') E_{ex}(x, y, z) E_{col}(x_a - x, y_a - y, z_a - z) dx dy dz. \end{aligned} \tag{3}$$

In addition to the signal, we need to consider the electric field distribution formed in the detection space by the excitation beam itself through the excitation system and signal-collection system, which functions as the local oscillator.

For simplicity, we consider the case of the condition $NA_{ex} = NA_{col}$. The image intensity $I^t(x', y', z')$ acquired by our imaging system can be written as

$$I^t(x', y', z') = \iiint | \{-iE_{ex}(x_a, y_a, z_a) + E_T(x', y', z'; x_a, y_a, z_a)\} |^2 a(x_a, y_a) \delta(z_a) dx_a dy_a dz_a, \tag{4}$$

where $a(x_a, y_a)$is the two-dimensional function representing the detector size, $\delta(z_a)$ stands for the Dirac delta function, the excitation beam $E_{ex}(x_a, y_a, z_a)$ acts as the local oscillator, and $-i$ before $E_{ex}(x_a, y_a, z_a)$ stems from the Gouy phase shift. To obtain the image intensity $I_c^t(x', y', z')$ for confocal microscopy, we can substitute $\delta(x_a)\,\delta(y_a)$ into $a(x_a, y_a)$ in Eq. (4). From Eqs. (3) and (4), we obtain

$$\begin{aligned} & I_c^t(x',y',z') \\ & = \left| -iE_{ex}(0,0,0) + \iiint \chi^{(1)}(x+x',y+y',z+z')E_{ex}(x,y,z)E_{col}(-x,-y,-z)dxdydz \right|^2 \\ & \approx \left| E_{ex}(0,0,0) \right|^2 \\ & \quad + i\left\{ E_{ex}(0,0,0) \right\}^* \iiint \chi^{(1)}(x+x',y+y',z+z')E_{ex}(x,y,z)E_{col}(-x,-y,-z)dxdydz \\ & \quad - iE_{ex}(0,0,0) \iiint \left\{ \chi^{(1)}(x+x',y+y',z+z') \right\}^* \left\{ E_{ex}(x,y,z) \right\}^* \left\{ E_{col}(-x,-y,-z) \right\}^* dxdydz. \end{aligned} \tag{5}$$

Although $E_{ex}(x, y, z)$ and $E_{col}(x, y, z)$ are complex functions, $E_{ex}(x, y, z)\,E_{col}(-x, -y, -z) \equiv \mathrm{ASF}_t(x, y, z)$ approaches a real function under the condition $\mathrm{NA}_{ex} = \mathrm{NA}_{col}$. Regarding $\mathrm{ASF}_t(x, y, z)$ as the real function, Eq. (5) reduces to

$$I_c^t(x',y',z') \approx \left| E_{ex}(0,0,0) \right|^2 - 2E_{ex}(0,0,0) \iiint \mathrm{Im}\{\chi^{(1)}(x+x',y+y',z+z')\}\mathrm{ASF}_t(x,y,z)dxdydz. \tag{6}$$

This equation shows that only absorbing objects can be observed and phase objects cannot be visualized. The first term in Eq. (6) leads to low-contrast images. The function $\mathrm{ASF}_t(x, y, z)$ is referred to as the amplitude spread function (ASF), and the coherent transfer function (CTF) is calculated by Fourier transforming the ASF.

2.3. Reflection linear confocal microscopy

Next, we deal with reflection linear confocal microscopy (see **Figure 4**), in which a $\chi^{(1)}$-derived optical process is harnessed. The excitation beam focused onto the sample by the excitation objective induces the polarization, and the signal generated from the polarization is gathered and delivered into a photodetector with the same objective. The excitation and signal-collection systems share a common objective. Unlike in transmission linear confocal microscopy, the excitation beam does not interfere with the signal. For reflection microscopy, the electric field distribution of the signal emitted from a single-point object in the sample $E_{col}(x_a, y_a, z_a)$ formed in the detection space through the signal-collection system is replaced by $E'_{col}(x_a, y_a, z_a)$, where the Fourier transform of $E'_{col}(x_a, y_a, z_a)$ is located on the $-k_z$ side (see **Figure 5**). With the arbitrary sample-stage displacement $(x', y' z')$, the electric field distribution $E_R(x', y' z'; x_a, y_a z_a)$ in the detection space is given by

$$E_{\mathrm{R}}(x',y',z';x_{\mathrm{a}},y_{\mathrm{a}},z_{\mathrm{a}}) = \iiint \chi^{(1)}(x+x',y+y',z+z')\,E_{\mathrm{ex}}(x,y,z)\,E'_{\mathrm{col}}(x_{\mathrm{a}}-x,y_{\mathrm{a}}-y,z_{\mathrm{a}}-z)dxdydz. \quad (7)$$

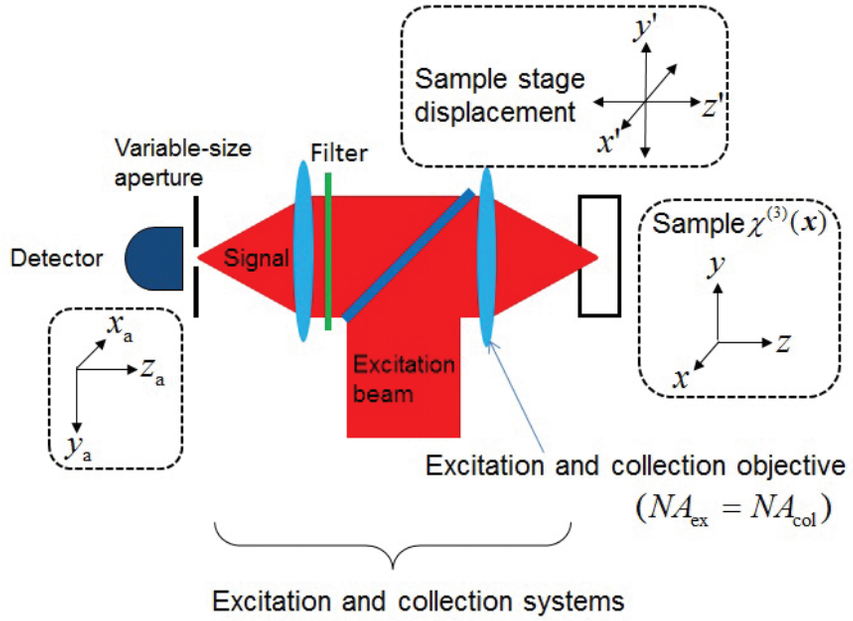

Figure 4. Schematic of reflection microscopy.

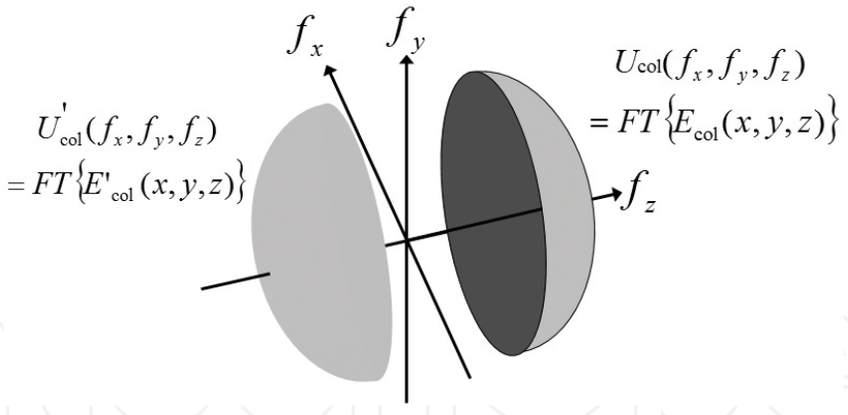

Figure 5. Distribution of the wavenumber vector (3-D pupil function) for the signal focused by the signal-collection objective.

As only the signal with no local oscillator forms the image, the image intensity $I_{\mathrm{c}}^{\mathrm{r}}(x',y',z')$ acquired by reflection linear confocal microscopy is written as

$$\begin{aligned} I_{\mathrm{c}}^{\mathrm{r}}(x',y',z') &= \iiint \left|\{E_{\mathrm{R}}(x',y',z';x_{\mathrm{a}},y_{\mathrm{a}},z_{\mathrm{a}})\}\right|^2 \delta(x_{\mathrm{a}})\delta(y_{\mathrm{a}})\delta(z_{\mathrm{a}})dx_{\mathrm{a}}dy_{\mathrm{a}}dz_{\mathrm{a}} \\ &= \left|\iiint \chi^{(1)}(x+x',y+y',z+z')E_{\mathrm{ex}}(x,y,z)E'_{\mathrm{col}}(-x,-y,-z)dxdydz\right|^2. \end{aligned} \quad (8)$$

The function $E_{ex}(x, y, z)E'_{col}(-x, -y, -z) \equiv ASF_r(x, y, z)$ is defined as the ASF for reflection linear confocal microscopy. Since we have the relation $E_{col}(x, y, z) = E'_{col}(-x, -y, -z)$, the ASF in reflection linear confocal microscopy $ASF_r(x, y, z)$ becomes equal to $E_{ex}(x, y, z)E_{col}(x, y, z)$. While the ASF in transmission linear confocal microscopy $ASF_t(x, y, z)$ approaches a real function, that in reflection linear confocal microscopy $ASF_r(x, y, z)$ is inevitably a complex function. In reflection linear confocal microscopy, the mixture image of the real and imaginary parts of the linear susceptibility is visualized.

2.4. Coherent nonlinear microscopy

We expand the image-forming formulas for $\chi^{(1)}$-derived optical processes to the general formulas for $\chi^{(i)}$-derived optical processes. In this subsection, we deal with coherent microscopy, which utilizes coherent optical processes. As an example, we first consider coherent anti-Stokes Raman scattering (CARS) microscopy, in which the two excitation beams (pump and Stokes) are used to generate the CARS signal (see **Figure 6**). In CARS microscopy, the pump and Stokes beams are temporally and spatially overlapped to generate the CARS signal such that the frequency difference between the pump and Stokes is tuned to match a particular Raman-active vibration frequency. The resonant CARS emission is several orders of magnitude greater than that from spontaneous Raman scattering. CARS microscopy provides chemically selective image contrast based on the intrinsic vibrational modes of molecular species, avoiding the need for labels. In addition, CARS imaging systems also employ near-infrared lasers to maximize imaging depth and minimize photodamage to cells. When the sample-stage displacement is zero, $(x', y', z') = (0, 0, 0)$, the polarization distribution becomes

$$P_{CARS}(x,y,z) = \chi^{(3)}_{CARS}(x,y,z)E_p(x,y,z)\{E_S(x,y,z)\}^* E_p(x,y,z), \tag{9}$$

where $\chi^{(3)}_{CARS}(x, y, z)$ denotes the nonlinear susceptibility for CARS and $E_p(x, y, z)$ and $E_s(x, y, z)$ stand for the electric field distributions in the sample formed by the pump and Stokes beams focused through the excitation system, respectively. In the same manner as in the previous subsection, taking into account the sample-stage displacement (x', y', z'), in transmission microscopy, the electric field distribution $E_{CARS}(x', y', z'; x_a, y_a, z_a)$ in the detection space can be written as

$$\begin{aligned} E_{CARS}(x',y',z';x_a,y_a,z_a) = \iiint \chi^{(3)}_{CARS}(x+x',y+y',z+z')E_p(x,y,z)\{E_S(x,y,z)\}^* E_p(x,y,z) \\ \times E_{col}(x_a-x,y_a-y,z_a-z)\,dxdydz, \end{aligned} \tag{10}$$

where $E_{col}(x, y, z)$ is calculated by using the wavelength of the CARS signal. Note that for reflection microscopy, $E_{col}(x, y, z)$ is replaced by $E'_{col}(x, y, z)$. As the wavelength of the CARS signal is different from those of the pump and Stokes beams, only the CARS signal can be

http://dx.doi.org/ 10.5772/63494

detected by using a filter. The image intensity $I_{\mathrm{CARS}}(x', y', z')$ acquired by CARS microscopy is given by

$$I_{\mathrm{CARS}}(x', y', z') = \iiint |\{E_{\mathrm{CARS}}(x', y', z'; x_{\mathrm{a}}, y_{\mathrm{a}}, z_{\mathrm{a}})\}|^2 \, a(x_{\mathrm{a}}, y_{\mathrm{a}})\delta(z_{\mathrm{a}})dx_{\mathrm{a}}dy_{\mathrm{a}}dz_{\mathrm{a}}. \tag{11}$$

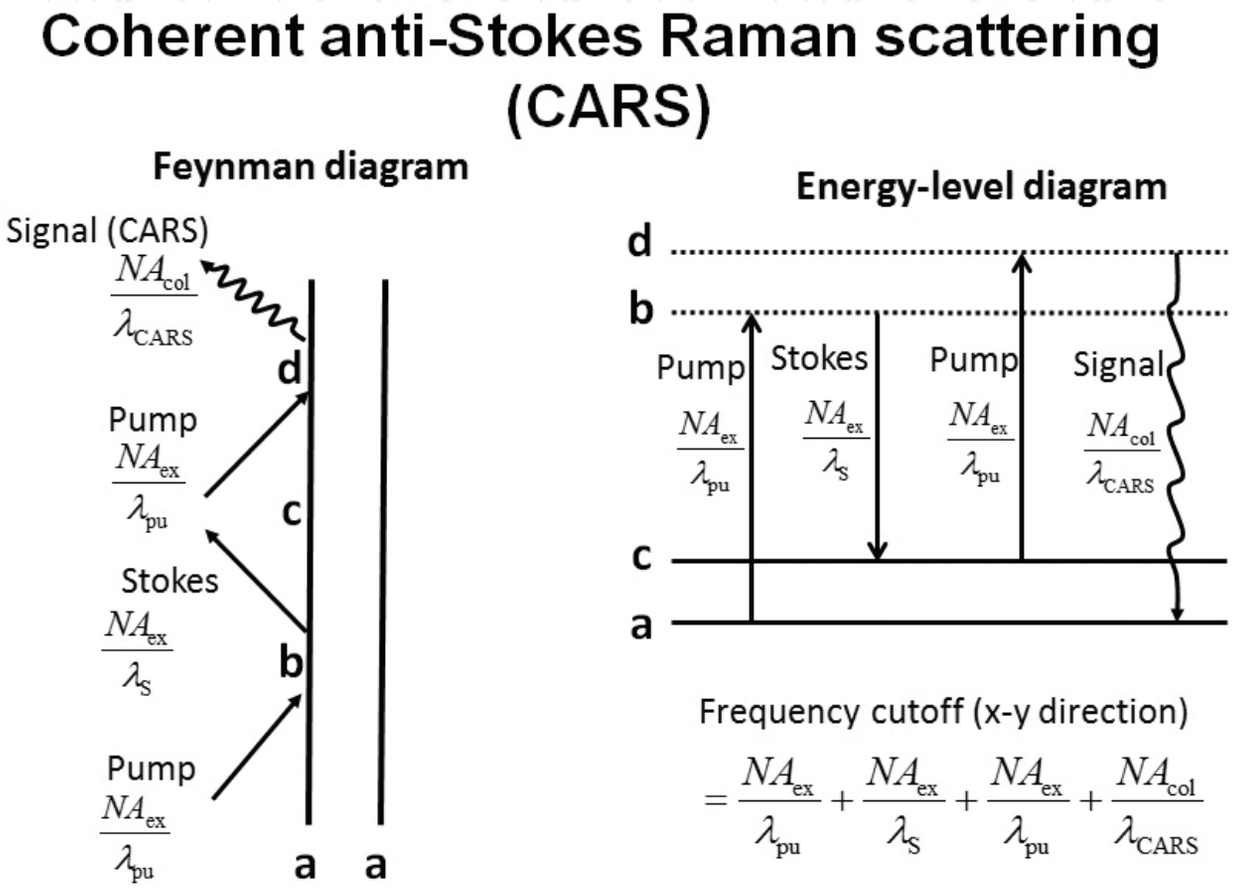

Figure 6. Double-sided Feynman diagram and energy-level diagram for CARS. λ_{pu} is the wavelength of the pump beam, λ_{S} is the wavelength of the Stokes beam, and λ_{CARS} is the wavelength of the CARS signal. The relation $2/\lambda_{\mathrm{pu}} - 1/\lambda_{\mathrm{S}} = 1/\lambda_{\mathrm{CARS}}$ is satisfied.

In confocal CARS microscopy, the image intensity $I^{\mathrm{c}}_{\mathrm{CARS}}(x', y', z')$ reduces to

$$\begin{aligned} I^{c}_{\mathrm{CARS}}(x', y', z') &= |\{E_{\mathrm{CARS}}(x', y', z'; 0, 0, 0)\}|^2 \\ &= \left| \iiint \chi^{(3)}_{\mathrm{CARS}}(x + x', y + y', z + z') E_p(x, y, z) \{E_S(x, y, z)\}^* E_p(x, y, z) E_{\mathrm{col}}(-x, -y, -z) dxdydz \right|^2 \\ &= \left| \iiint \chi^{(3)}_{\mathrm{CARS}}(x + x', y + y', z + z') \mathrm{ASF}_{\mathrm{CARS}}(x, y, z) dxdydz \right|^2 . \end{aligned} \tag{12}$$

where $\mathrm{ASF}_{\mathrm{CARS}}(x, y, z) \equiv E_{\mathrm{p}}(x, y, z)\{E_{\mathrm{S}}(x, y, z)\}^* E_{\mathrm{p}}(x, y, z) E_{\mathrm{col}}(-x, -y, -z)$. The CTF of CARS microscopy is calculated by Fourier transforming $\mathrm{ASF}_{\mathrm{CARS}}(x, y, z)$. The maximum value of the

frequency cutoff, which means the grating with the largest grating vector that can be resolved, is determined by the CTF. It is proven that the frequency cutoff of nonconfocal CARS microscopy does not change compared with that of confocal CARS microscopy [4]. In general, in coherent microscopy, the theoretical resolution limits (frequency cutoffs) are identical between confocal and nonconfocal systems.

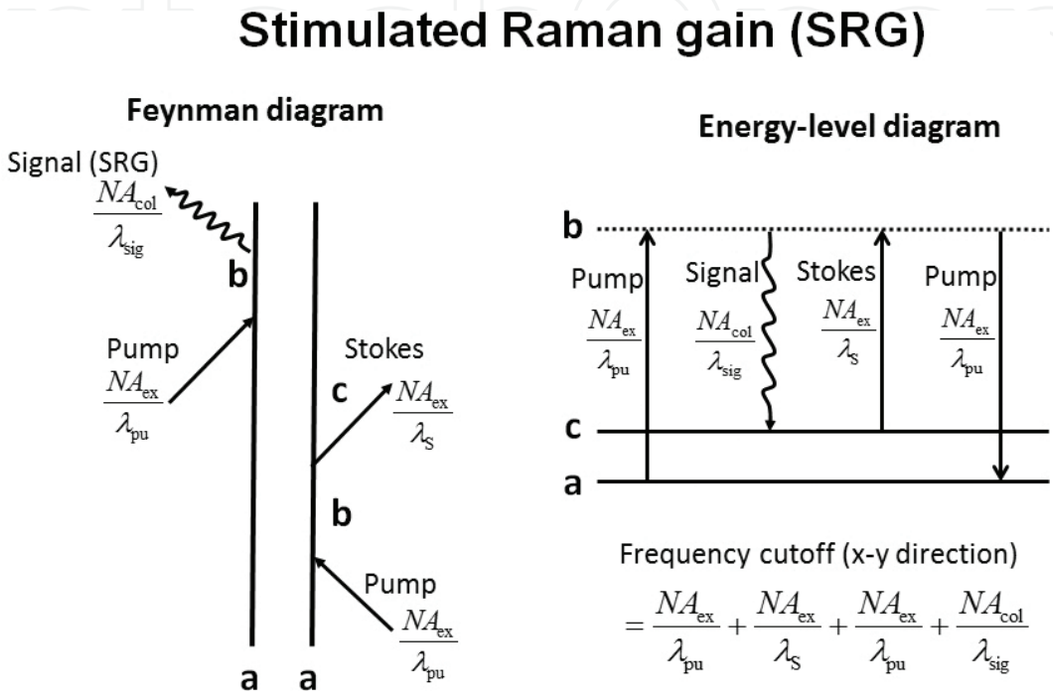

Figure 7. Double-sided Feynman diagram and energy-level diagram for SRG. λ_{sig} is the wavelength of the SRG signal. Note that $\lambda_S = \lambda_{sig}$.

As the next example, we consider stimulated Raman gain (SRG) microscopy, in which the pump and Stokes beams are employed as the excitation beams in common with CARS microscopy. As the wavelength of the SRG signal is identical with that of the Stokes beam (see **Figure 7**), the SRG signal interferes with the Stokes beam, which acts as the local oscillator in transmission microscopy. The pump beam is modulated and the SRG signal with the same wavelength as the Stokes beam can be extracted by demodulating the Stokes beam with the lock-in amplifier. In the signal-collection system, the pump beam is blocked by the filter. When $(x', y', z') = (0, 0, 0)$, the polarization distribution is given by

$$P_{\mathrm{SRG}}(x,y,z) = \chi^{(3)}_{\mathrm{SRG}}(x,y,z)\{E_p(x,y,z)\}^* E_S(x,y,z)E_p(x,y,z), \tag{13}$$

where $\chi^{(3)}_{\mathrm{SRG}}(x, y, z)$ represents the nonlinear susceptibility for SRG. With the sample-stage displacement (x', y', z'), in transmission microscopy, the electric field distribution of the SRG signal $E_{\mathrm{SRG}}(x', y', z'; x_a, y_a, z_a)$ in the detection space is written as

$$E_{\mathrm{SRG}}(x',y',z';x_a,y_a,z_a)=\iiint \chi^{(3)}_{\mathrm{SRG}}(x+x',y+y',z+z')\{E_p(x,y,z)\}^* E_S(x,y,z)E_p(x,y,z) \times E_{\mathrm{col}}(x_a-x,y_a-y,z_a-z)dxdydz, \tag{14}$$

where $E_{\mathrm{col}}(x, y, z)$ in this case must be calculated by using the wavelength of the SRG signal. With the filter that blocks the pump beam, the total intensity $I^{t}_{\mathrm{SRG}}(x', y', z')$ identified by the detector of transmission SRG microscopy is given by

$$I^{t}_{\mathrm{SRG}}(x',y',z')=\iiint |-iE_S(x_a,y_a,z_a)+E_{\mathrm{SRG}}(x',y',z';x_a,y_a,z_a)|^2 a(x_a,y_a)\delta(z_a)dx_a dy_a dz_a, \tag{15}$$

where the Stoke beam $-iE_S(x_a, y_a, z_a)$ with the Gouy phase shift $(-i)$ functions as the local oscillator. In confocal transmission SRG microscopy, substituting $\delta(x_a)$ $\delta(y_a)$ into $a(x_a, y_a)$, $I^{t}_{\mathrm{SRG}}(x', y', z')$ reduces to

$$\begin{aligned}
&I^{ct}_{\mathrm{SRG}}(x',y',z')\\
&=\Big|-iE_S(0,0,0)+\iiint \chi^{(3)}_{\mathrm{SRG}}(x+x',y+y',z+z')\\
&\qquad\times\{E_p(x,y,z)\}^* E_S(x,y,z)E_p(x,y,z)E_{\mathrm{col}}(-x,-y,-z)dxdydz\Big|^2\\
&\approx |E_S(0,0,0)|^2\\
&+i\{E_S(0,0,0)\}^*\iiint \chi^{(3)}_{\mathrm{SRG}}(x+x',y+y',z+z')|E_p(x,y,z)|^2 E_S(x,y,z)E_{\mathrm{col}}(-x,-y,-z)dxdydz\\
&-iE_S(0,0,0)\iiint\{\chi^{(3)}_{\mathrm{SRG}}(x+x',y+y',z+z')\}^* |E_p(x,y,z)|^2\{E_S(x,y,z)\}^*\\
&\qquad\times\{E_{\mathrm{col}}(-x,-y,-z)\}^* dxdydz\\
&=|E_S(0,0,0)|^2-2E_S(0,0,0)\iiint \mathrm{Im}\{\chi^{(3)}_{\mathrm{SRG}}(x+x',y+y',z+z')\}ASF_{\mathrm{SRG}}(x,y,z)dxdydz,
\end{aligned} \tag{16}$$

where we used the fact that $\mathrm{ASF}_{\mathrm{SRG}}(x, y, z) \equiv |E_p(x, y, z)|^2 E_S(x, y, z)E_{\mathrm{col}}(-x, -y, -z)$ approaches a real function under the condition $\mathrm{NA}_{ex} = \mathrm{NA}_{\mathrm{col}}$. Note that the sign of $\mathrm{Im}\{\chi^{(3)}_{\mathrm{SRG}}\}$ is negative in SRG. The first term in Eq. (16) can be eliminated with lock-in detection. The CTF is calculated by Fourier transforming $\mathrm{ASF}_{\mathrm{SRG}}(x, y, z)$.

We also consider "nonconfocal" transmission SRG microscopy, which is normally used to achieve a high signal intensity. Although the detector is normally placed at the plane conjugate to the pupil of the collection objective in nonconfocal microscopy, we deal with microscopy in which the detector is placed at the image plane conjugate to the sample plane to discuss confocal microscopy and nonconfocal microscopy in the same theoretical framework. Note that in nonconfocal microscopy, the image does not change regardless of detector position. Therefore, to simplify the equation, we calculate the intensity value at a certain sample-stage displacement (x', y', z') by three-dimensionally integrating the signal intensity in the detection

space. The image intensity is proportional to the above-mentioned calculation result. The image intensity $I_{\mathrm{SRG}}^{\mathrm{nct}}(x', y', z')$ acquired by the detector of nonconfocal transmission SRG microscopy is given by

$$
\begin{aligned}
&I_{\mathrm{SRG}}^{\mathrm{nct}}(x',y',z') \\
&\propto \iiint \left|\left\{-iE_{\mathrm{S}}(x_{\mathrm{a}},y_{\mathrm{a}},z_{\mathrm{a}})+E_{\mathrm{SRG}}(x',y',z';x_{\mathrm{a}},y_{\mathrm{a}},z_{\mathrm{a}})\right\}\right|^2 dx_{\mathrm{a}}dy_{\mathrm{a}}dz_{\mathrm{a}} \\
&= \iiint [\left|E_{\mathrm{S}}(x_{\mathrm{a}},y_{\mathrm{a}},z_{\mathrm{a}})\right|^2 + i\left\{E_{\mathrm{S}}(x_{\mathrm{a}},y_{\mathrm{a}},z_{\mathrm{a}})\right\}^* \\
&\quad \times \iiint \chi_{\mathrm{SRG}}^{(3)}(x+x',y+y',z+z')\left|E_{\mathrm{p}}(x,y,z)\right|^2 E_{\mathrm{S}}(x,y,z)E_{\mathrm{col}}(x_{\mathrm{a}}-x,y_{\mathrm{a}}-y,z_{\mathrm{a}}-z)dxdydz \\
&\quad -iE_{\mathrm{S}}(x_{\mathrm{a}},y_{\mathrm{a}},z_{\mathrm{a}})\iiint \chi_{\mathrm{SRG}}^{(3)}(x+x',y+y',z+z')\left|E_{\mathrm{p}}(x,y,z)\right|^2\left\{E_{\mathrm{S}}(x,y,z)\right\}^* \\
&\quad \times\left\{E_{\mathrm{col}}(x_{\mathrm{a}}-x,y_{\mathrm{a}}-y,z_{\mathrm{a}}-z)\right\}^* dxdydz]dx_{\mathrm{a}}dy_{\mathrm{a}}dz_{\mathrm{a}} \\
&= \iiint \left|E_{\mathrm{S}}(x_{\mathrm{a}},y_{\mathrm{a}},z_{\mathrm{a}})\right|^2 dx_{\mathrm{a}}dy_{\mathrm{a}}dz_{\mathrm{a}} \\
&\quad + i\iiint \chi_{\mathrm{SRG}}^{(3)}(x+x',y+y',z+z')\left|E_{\mathrm{p}}(x,y,z)\right|^2\left|E_{\mathrm{S}}(x,y,z)\right|^2 dxdydz \\
&\quad - i\iiint \left\{\chi_{\mathrm{SRG}}^{(3)}(x+x',y+y',z+z')\right\}^*\left|E_{\mathrm{p}}(x,y,z)\right|^2\left|E_{\mathrm{S}}(x,y,z)\right|^2 dxdydz \\
&= \iiint \left|E_{\mathrm{S}}(x_{\mathrm{a}},y_{\mathrm{a}},z_{\mathrm{a}})\right|^2 dx_{\mathrm{a}}dy_{\mathrm{a}}dz_{\mathrm{a}} \\
&\quad -2\iiint \mathrm{Im}\left\{\chi_{\mathrm{SRG}}^{(3)}(x+x',y+y',z+z')\right\}^*\left|E_{\mathrm{p}}(x,y,z)\right|^2\left|E_{\mathrm{S}}(x,y,z)\right|^2 dxdydz.
\end{aligned}
\tag{17}
$$

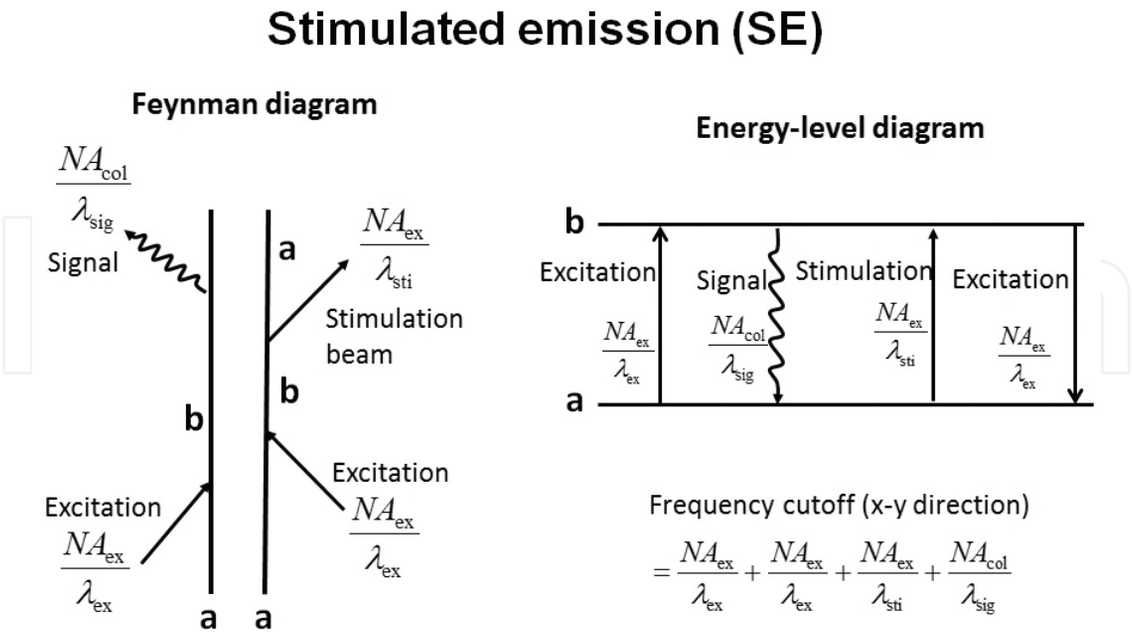

Figure 8. Double-sided Feynman diagram and energy-level diagram for stimulated emission. λ_{ex} is the wavelength of the excitation beam, λ_{sti} is the wavelength of the stimulation beam, and λ_{sig} is the wavelength of the SE signal. A two-level system is assumed.

Here we used the relations $E_{col}(-x, -y, -z) = \{E_{col}(x, y, z)\}^*$ and $E_S(x_a, y_a, z_a) \otimes E_{col}(x_a, y_a, z_a) = E_S(x_a, y_a, z_a)$ under the condition $NA_{ex} = NA_{col}$, where $\otimes$ represents the convolution. The first term in Eq. (17) can be eliminated with lock-in detection. The ASF for nonconfocal SRG microscopy is $|E_p(x, y, z)|^2 |E_S(x, y, z)|^2$, which is nearly equal to the ASF for confocal microscopy.

We then consider nonconfocal reflection SRG microscopy. Interestingly, in nonconfocal reflection SRG microscopy, the reflection light $E_R(x', y', z'; x_a, y_a z_a)$ generated by the $\chi^{(1)}$-derived optical process plays a role as the local oscillator. The image intensity $I_{SRG}^{ncr}(x', y', z')$ acquired by the detector of nonconfocal reflection SRG microscopy is given by

$$\begin{aligned}
&I_{SRG}^{ncr}(x', y', z') \\
&\propto \iiint \left| \left\{ E_R(x', y', z'; x_a, y_a, z_a) + E_{SRG}(x', y', z'; x_a, y_a, z_a) \right\} \right|^2 dx_a dy_a dz_a \\
&= \iiint \left| \iiint \chi^{(1)}(x + x', y + y', z + z') E_S(x, y, z) E'_{col}(x_a - x, y_a - y, z_a - z) dx dy dz \right. \\
&\quad + \iiint \chi_{SRG}^{(3)}(x + x', y + y', z + z') \left\{ E_p(x, y, z) \right\}^* E_S(x, y, z) E_p(x, y, z) \\
&\quad \left. \times E'_{col}(x_a - x, y_a - y, z_a - z) dx dy dz \right|^2 dx_a dy_a dz_a .
\end{aligned} \tag{18}$$

As the local oscillator in this case does not have a Gouy phase shift, the real part of $\chi_{SRG}^{(3)}(x, y, z)$ is mainly observed. To see this, we consider a single-point object: $\chi^{(1)}(x, y, z) = \delta(x, y, z)$ and $\chi_{SRG}^{(3)}(x, y, z) = \varepsilon_r \delta(x, y, z) + i\varepsilon_i \delta(x, y, z)$, where $\varepsilon_r, \varepsilon_i \ll 1$. Eq. (18) reduces to

$$\begin{aligned}
&I_{SRG}^{ncr} \\
&\propto \iiint \left| E_S(-x', -y', -z') E'_{col}(x_a + x', y_a + y', z_a + z') \right. \\
&\quad + \varepsilon_r \left| E_p(-x', -y', -z') \right|^2 E_S(-x', -y', -z') E'_{col}(x_a + x', y_a + y', z_a + z') \\
&\quad \left. + i\varepsilon_i \left| E_p(-x', -y', -z') \right|^2 E_S(-x', -y', -z') E'_{col}(x_a + x', y_a + y', z_a + z') \right|^2 dx_a dy_a dz_a \\
&\approx \left| E_S(-x', -y', -z') \right|^2 \iiint \left| E'_{col}(x_a, y_a, z_a) \right|^2 dx_a dy_a dz_a \\
&\quad + 2\varepsilon_r \iiint \left| E'_{col}(x_a, y_a, z_a) \right|^2 dx_a dy_a dz_a \, \mathrm{Re} \left\{ \left| E_p(-x', -y', -z') \right|^2 \left| E_S(-x', -y', -z') \right|^2 \right\} \\
&\quad - 2\varepsilon_i \iiint \left| E'_{col}(x_a, y_a, z_a) \right|^2 dx_a dy_a dz_a \, \mathrm{Im} \left\{ \left| E_p(-x', -y', -z') \right|^2 \left| E_S(-x', -y', -z') \right|^2 \right\}.
\end{aligned} \tag{19}$$

The third term in Eq. (19) becomes zero, and the first term can be eliminated with lock-in detection. Eventually, only the real part ε_r remains.

The last example for coherent nonlinear microscopy is stimulated emission (SE) microscopy, in which the pump beam (electric field distribution: $E_p(x, y, z)$) and the stimulation beam (electric field distribution: $E_{sti}(x, y, z)$) are employed to generate the signal (see **Figure 8**). In SE microscopy, the SE signal has the same wavelength as that of the stimulation beam, and the SE signal interferes with the stimulation beam, which functions as the local oscillator in transmission microscopy. The pump beam is modulated and the SE signal can be extracted by demodulating the stimulation beam interfering with the SE signal. In analogy with SRG microscopy, replacing $E_S(x_a, y_a, z_a)$ with $E_{sti}(x_a, y_a, z_a)$ and $E_{SRG}(x', y', z'; x_a, y_a, z_a)$ by $E_{SE}(x', y', z'; x_a, y_a, z_a) \equiv \iiint \chi_{SE}^{(3)}(x+x', y+y', z+z') \mid E_p(x, y, z) \mid^2 E_{sti}(x, y, z)\, E_{col}(x_a\text{-}x, y_a\text{-}y, z_a\text{-}z) d_x d_y d_z$, the image intensity $I_{SE}^{nct}(x', y', z')$ acquired by the detector in nonconfocal transmission SE microscopy is written as

$$
\begin{aligned}
& I_{SE}^{nct} \\
& \propto \iiint \left| \left\{ -iE_{sti}(x_a, y_a, z_a) + E_{SE}(x', y', z'; x_a, y_a, z_a) \right\} \right|^2 dx_a dy_a dz_a \\
& = \iiint \Big[\left| E_{sti}(x_a, y_a, z_a) \right|^2 + i \left\{ E_{sti}(x_a, y_a, z_a) \right\}^* \\
& \quad \times \iiint \chi_{SE}^{(3)}(x+x', y+y', z+z') \left| E_p(x, y, z) \right|^2 E_{sti}(x, y, z) E_{col}(x_a - x, y_a - y, z_a - z)\, dxdydz \\
& \quad - iE_{sti}(x_a, y_a, z_a) \iiint \left\{ \chi_{SE}^{(3)}(x+x', y+y', z+z') \right\}^* \left| E_p(x, y, z) \right|^2 \left\{ E_{sti}(x, y, z) \right\}^* \\
& \quad \times \left\{ E_{col}(x_a - x, y_a - y, z_a - z) \right\}^* dxdydz \Big] dx_a dy_a dz_a \\
& = \iiint \left| E_{sti}(x_a, y_a, z_a) \right|^2 dx_a dy_a dz_a \\
& \quad + i \iiint \chi_{SE}^{(3)}(x+x', y+y', z+z') \left| E_p(x, y, z) \right|^2 \left| E_{sti}(x, y, z) \right|^2 dxdydz \\
& \quad - i \iiint \left\{ \chi_{SE}^{(3)}(x+x', y+y', z+z') \right\}^* \left| E_p(x, y, z) \right|^2 \left| E_{sti}(x, y, z) \right|^2 dxdydz \\
& = \iiint \left| E_{sti}(x_a, y_a, z_a) \right|^2 dx_a dy_a dz_a \\
& \quad - 2 \iiint \mathrm{Im} \left\{ \chi_{SE}^{(3)}(x+x', y+y', z+z') \right\} \left| E_p(x, y, z) \right|^2 \left| E_{sti}(x, y, z) \right|^2 dxdydz,
\end{aligned}
\tag{20}
$$

where $\chi_{SE}^{(3)}(x, y, z)$ represents the nonlinear susceptibility for SE. In Eq. (20), we used the relations $E_{col}(-x, -y, -z) = \{E_{col}(x, y, z)\}^*$ and $E_{sti}(x_a, y_a, z_a) \otimes E_{col}(x_a, y_a, z_a) = E_{sti}(x_a, y_a, z_a)$ under the condition $NA_{ex} = NA_{col}$. The first term can be eliminated with lock-in detection. The ASF for nonconfocal SE microscopy is $\mid E_p(x, y, z) \mid^2 \mid E_{sti}(x, y, z) \mid^2$, which is nearly equal to the

ASF for confocal microscopy. Although this equation for SE microscopy is described by the same notation as SRG microscopy, the Feynman diagram differs.

2.5. Incoherent microscopy

To deal with incoherent optical processes, the vacuum field around the sample needs to be reckoned in our calculation. We assume that $|0\rangle_{(x,y,z)}$ denotes the amplitude of the quantum vacuum zero-point effect at the (x,y,z) position in the sample. For spontaneous Raman scattering, the Stokes beam $E_S(x_a, y_a, z_a)$ is replaced by the vacuum field $|0\rangle_{(x_a,y_a,z_a)}$:

$$\begin{aligned} & I_{\mathrm{Ra}}^{\mathrm{t}}(x',y',z') \\ &= \iiint \left| -i|0\rangle_{(x_a,y_a,z_a)} + E_{\mathrm{SRG}}(x',y',z';x_a,y_a,z_a) \right|^2 a(x_a,y_a)\delta(z_a)dx_a dy_a dz_a \\ &= \iiint \left| -i|0\rangle_{(x_a,y_a,z_a)} + \iiint \chi_{\mathrm{SRG}}^{(3)}(x+x',y+y',z+z')\{E_{\mathrm{p}}(x,y,z)\}^* E_{\mathrm{p}}(x,y,z)|0\rangle_{(x,y,z)} \right. \\ &\quad \left. \times E_{\mathrm{col}}(x_a-x,y_a-y,z_a-z)dxdydz \right|^2 a(x_a,y_a)\delta(z_a)dx_a dy_a dz_a. \end{aligned} \tag{21}$$

We then consider the Fourier expansion of $|0\rangle_{(x,y,z)}$ into the plane wave basis $|0\rangle_{(k_x,k_y,k_z)}$:

$$|0\rangle_{(x,y,z)} = \frac{1}{(2\pi)^3}\iiint |0\rangle_{(k_x,k_y,k_z)} e^{-i(k_x x+k_y y+k_z z)} dk_x dk_y dk_z, \tag{22}$$

$$|0\rangle_{(x_a,y_a,z_a)} = \frac{1}{(2\pi)^3}\iiint C(k_x,k_y,k_z)|0\rangle_{(k_x,k_y,k_z)} e^{-i(k_x x_a+k_y y_a+k_z z_a)} dk_x dk_y dk_z, \tag{23}$$

where (k_x, k_y, k_z) is the wavenumber vector, $|0\rangle_{(k_x,k_y,k_z)}$ stands for the Fourier component of the vacuum field, and $C(k_x, k_y, k_z)$ is the cone-shaped function representing the wave vectors of the Fourier components of the vacuum field that can pass through the signal-collection objective with NA_{col} and reach the detector. In the case of the fixed angular frequency of the

pump, the nonlinear susceptibility of SRG is a function of the angular frequency of the Stokes beam: $\omega_S = c\sqrt{k_x^2 + k_y^2 + k_z^2}$, where c is the light speed in vacuum. Therefore, we can replace $\chi^{(3)}_{\mathrm{SRG}}(x, y, z)$ in Eq. (21) with $\chi^{(3)}_{\mathrm{SRG}}(x, y, z)L\,(k_x, k_y, k_z)$, where $L\,(k_x, k_y, k_z)$ is a spherically symmetrical function (typically a complex Lorentzian function of ω_S). We then obtain

$$I^t_{\mathrm{Ra}}(x', y', z') = \iiint |\, A_{\mathrm{Ra}}(x', y', z'; x_a, y_a, z_a)\,|^2\; a(x_a, y_a)\delta(z_a)dx_a dy_a dz_a, \tag{24}$$

with

$$\begin{aligned}
&\left|A_{\mathrm{Ra}}\left(x', y', z'; x_{\mathrm{a}}, y_{\mathrm{a}}, z_{\mathrm{a}}\right)\right|^2 \\
&= \Big| -i\,|0\rangle_{(x_{\mathrm{a}}, y_{\mathrm{a}}, z_{\mathrm{a}})} + \iiint \chi^{(3)}_{\mathrm{SRG}}\left(x + x', y + y', z + z'\right) L\left(k_x, k_y, k_z\right)\left\{E_{\mathrm{p}}\left(x, y, z\right)\right\}^* E_{\mathrm{p}}\left(x, y, z\right) \\
&\quad \times |0\rangle_{(x,y,z)} E_{\mathrm{col}}\left(x_{\mathrm{a}} - x, y_{\mathrm{a}} - y, z_{\mathrm{a}} - z\right) dxdydz \Big|^2 \\
&= \Bigg| -i\frac{1}{(2\pi)^3}\iiint C\left(k_x, k_y, k_z\right)|0\rangle_{(k_x,k_y,k_z)} e^{-i\left(k_x x_{\mathrm{a}} + k_y y_{\mathrm{a}} + k_z z_{\mathrm{a}}\right)} dk_x dk_y dk_z \\
&\quad + \iiint \chi^{(3)}_{\mathrm{SRG}}\left(x + x', y + y', z + z'\right) L\left(k_x, k_y, k_z\right)\left\{E_{\mathrm{p}}\left(x, y, z\right)\right\}^* E_{\mathrm{p}}\left(x, y, z\right) \\
&\quad \times \frac{1}{(2\pi)^3}\iiint |0\rangle_{(k_x,k_y,k_z)} e^{-i\left(k_x x + k_y y + k_z z\right)} dk_x dk_y dk_z\, E_{\mathrm{col}}\left(x_{\mathrm{a}} - x, y_{\mathrm{a}} - y, z_{\mathrm{a}} - z\right) dxdydz \Bigg|^2 \\
&\approx \frac{1}{(2\pi)^6}\iiint\iiint C\left(k_x, k_y, k_z\right) C^*\left(k'_x, k'_y, k'_z\right)_{(k'_x,k'_y,k'_z)} \langle 0|0\rangle_{(k_x,k_y,k_z)} e^{-i\left\{\left(k_x - k'_x\right)x_{\mathrm{a}} + \left(k_y - k'_y\right)y_{\mathrm{a}} + \left(k_z - k'_z\right)z_{\mathrm{a}}\right\}} \\
&\quad \times dk_x dk_y dk_z dk'_x dk'_y dk'_z \\
&\quad + i\frac{1}{(2\pi)^6}\iiint\iiint\iiint L\left(k_x, k_y, k_z\right) C^*\left(k'_x, k'_y, k'_z\right)_{(k'_x,k'_y,k'_z)} \langle 0|0\rangle_{(k_x,k_y,k_z)} e^{i\left(k_x x_{\mathrm{a}} + k_y y_{\mathrm{a}} + k_z z_{\mathrm{a}}\right)} \\
&\quad \times e^{-i\left(k'_x x + k'_y y + k'_z z\right)} dk_x dk_y dk_z dk'_x dk'_y dk'_z\; \chi^{(3)}_{\mathrm{SRG}}\left(x + x', y + y', z + z'\right)\left|E_{\mathrm{p}}\left(x, y, z\right)\right|^2 \\
&\quad \times E_{\mathrm{col}}\left(x_{\mathrm{a}} - x, y_{\mathrm{a}} - y, z_{\mathrm{a}} - z\right) dxdydz \qquad + \text{c.c.}
\end{aligned} \tag{25}$$

In common with SRG, the fourth term in the above equation is negligible also in spontaneous Raman scattering. Thus, we omitted the fourth term. Carrying on the calculation, we obtain

$$
\begin{aligned}
&\left|A_{\mathrm{Ra}}\left(x',y',z';x_{\mathrm{a}},y_{\mathrm{a}},z_{\mathrm{a}}\right)\right|^2\\
&=\frac{1}{(2\pi)^3}\iiint\iiint C\left(k_x,k_y,k_z\right)P^*\left(k_x',k_y',k_z'\right)\delta\left(k_x-k_x'\right)\delta\left(k_y-k_y'\right)\delta\left(k_z-k_z'\right)\\
&\quad\times e^{-i\left\{\left(k_x-k_x'\right)x_{\mathrm{a}}+\left(k_y-k_y'\right)y_{\mathrm{a}}+\left(k_z-k_z'\right)z_{\mathrm{a}}\right\}}dk_xdk_ydk_zdk_x'dk_y'dk'\\
&\quad+i\frac{1}{(2\pi)^3}\iiint\iiint\iiint L\left(k_x,k_y,k_z\right)C^*\left(k_x',k_y',k_z'\right)\delta\left(k_x-k_x'\right)\delta\left(k_y-k_y'\right)\delta\left(k_z-k_z'\right)\\
&\quad\times e^{i\left(k_xx_{\mathrm{a}}+k_yy_{\mathrm{a}}+k_zz_{\mathrm{a}}\right)}e^{-i\left(k_x'x+k_y'y+k_z'z\right)}dk_xdk_ydk_zdk_x'dk_y'dk_z'\ \chi^{(3)}_{\mathrm{SRG}}\left(x+x',y+y',z+z'\right)\\
&\quad\times\left|E_{\mathrm{p}}\left(x,y,z\right)\right|^2E_{\mathrm{col}}\left(x_{\mathrm{a}}-x,y_{\mathrm{a}}-y,z_{\mathrm{a}}-z\right)dxdydz\qquad+\text{c.c.}\\
&=\frac{1}{(2\pi)^3}\iiint\left|C\left(k_x,k_y,k_z\right)\right|^2dk_xdk_ydk_z\\
&\quad+i\frac{1}{(2\pi)^3}\iiint\iiint L\left(k_x,k_y,k_z\right)C^*\left(k_x',k_y',k_z'\right)e^{-i\left\{\left(x-x_{\mathrm{a}}\right)k_x+\left(y-y_{\mathrm{a}}\right)k_y+\left(z-z_{\mathrm{a}}\right)k_z\right\}}dk_xdk_ydk_z\\
&\quad\times\chi^{(3)}_{\mathrm{SRG}}\left(x+x',y+y',z+z'\right)\left|E_{\mathrm{p}}\left(x,y,z\right)\right|^2E_{\mathrm{col}}\left(x_{\mathrm{a}}-x,y_{\mathrm{a}}-y,z_{\mathrm{a}}-z\right)dxdydz\qquad+\text{c.c.}\\
&=\frac{1}{(2\pi)^3}\iiint\left|C\left(k_x,k_y,k_z\right)\right|^2dk_xdk_ydk_z\\
&\quad+i\iiint\chi^{(3)}_{\mathrm{SRG}}\left(x+x',y+y',z+z'\right)\left|E_{\mathrm{p}}\left(x,y,z\right)\right|^2\left|E_{\mathrm{col}}\left(x_{\mathrm{a}}-x,y_{\mathrm{a}}-y,z_{\mathrm{a}}-z\right)\right|^2dxdydz\qquad+\text{c.c.}\\
&=\frac{1}{(2\pi)^3}\iiint\left|C\left(k_x,k_y,k_z\right)\right|^2dk_xdk_ydk_z\\
&\quad-2\iiint\mathrm{Im}\left\{\chi^{(3)}_{\mathrm{SRG}}\left(x+x',y+y',z+z'\right)\right\}\left|E_{\mathrm{p}}\left(x,y,z\right)\right|^2\left|E_{\mathrm{col}}\left(x_{\mathrm{a}}-x,y_{\mathrm{a}}-y,z_{\mathrm{a}}-z\right)\right|^2dxdydz.
\end{aligned}
\tag{26}
$$

Here we used the following equations:

$$
\left(k_x',k_y',k_z'\right)^{\langle 0|0\rangle_{\left(k_x,k_y,k_z\right)}}=(2\pi)^3\,\delta\left(k_x-k_x'\right)\delta\left(k_y-k_y'\right)\delta\left(k_z-k_z'\right),
\tag{27}
$$

$$
\begin{aligned}
&\frac{1}{(2\pi)^3}\iiint L\left(k_x,k_y,k_z\right)C^*\left(k_x,k_y,k_z\right)e^{-i\left\{\left(x-x_{\mathrm{a}}\right)k_x+\left(y-y_{\mathrm{a}}\right)k_y+\left(z-z_{\mathrm{a}}\right)k_z\right\}}dk_xdk_ydk_z\\
&=E^*_{\mathrm{col}}\left(x_{\mathrm{a}}-x,y_{\mathrm{a}}-y,z_{\mathrm{a}}-z\right).
\end{aligned}
\tag{28}
$$

The first term in Eq. (26) corresponds to the vacuum field that cannot be observed. As only the difference from the vacuum state can be measured, the detected signal becomes

$$
\begin{aligned}
&I^{\mathrm{de}}_{\mathrm{Ra}}\left(x',y',z'\right)\approx\\
&\iiint\left\{\iiint\mathrm{Im}\left\{-2\,\chi^{(3)}_{\mathrm{SRG}}\left(x+x',y+y',z+z'\right)\right\}\left|E_{\mathrm{p}}\left(x,y,z\right)\right|^2\left|E_{\mathrm{col}}\left(x_{\mathrm{a}}-x,y_{\mathrm{a}}-y,z_{\mathrm{a}}-z\right)\right|^2dxdydz\right\}\\
&\quad\times a\left(x_{\mathrm{a}},y_{\mathrm{a}}\right)\delta\left(z_{\mathrm{a}}\right)dx_{\mathrm{a}}dy_{\mathrm{a}}dz_{\mathrm{a}}.
\end{aligned}
\tag{29}
$$

Note that $\mathrm{Im}\{\chi^{(3)}_{\mathrm{SRG}}(x, y, z)\}$ is a negative value. This equation is well known as the image-forming formula of confocal microscopy with a finite detector size for incoherent optical processes [12]. In incoherent microscopy, the size of the detector influences the optical resolution, according to Eq. (29). In nonconfocal incoherent microscopy, only the pump beam $|E_{\mathrm{p}}(x, y, z)|^2$ determines the optical resolution, while in confocal incoherent microscopy, both the pump beam $|E_{\mathrm{p}}(x, y, z)|^2$ and the signal $|E_{\mathrm{col}}(-x, -y, -z)|^2$ affect the resolution limit, resulting in better resolution.

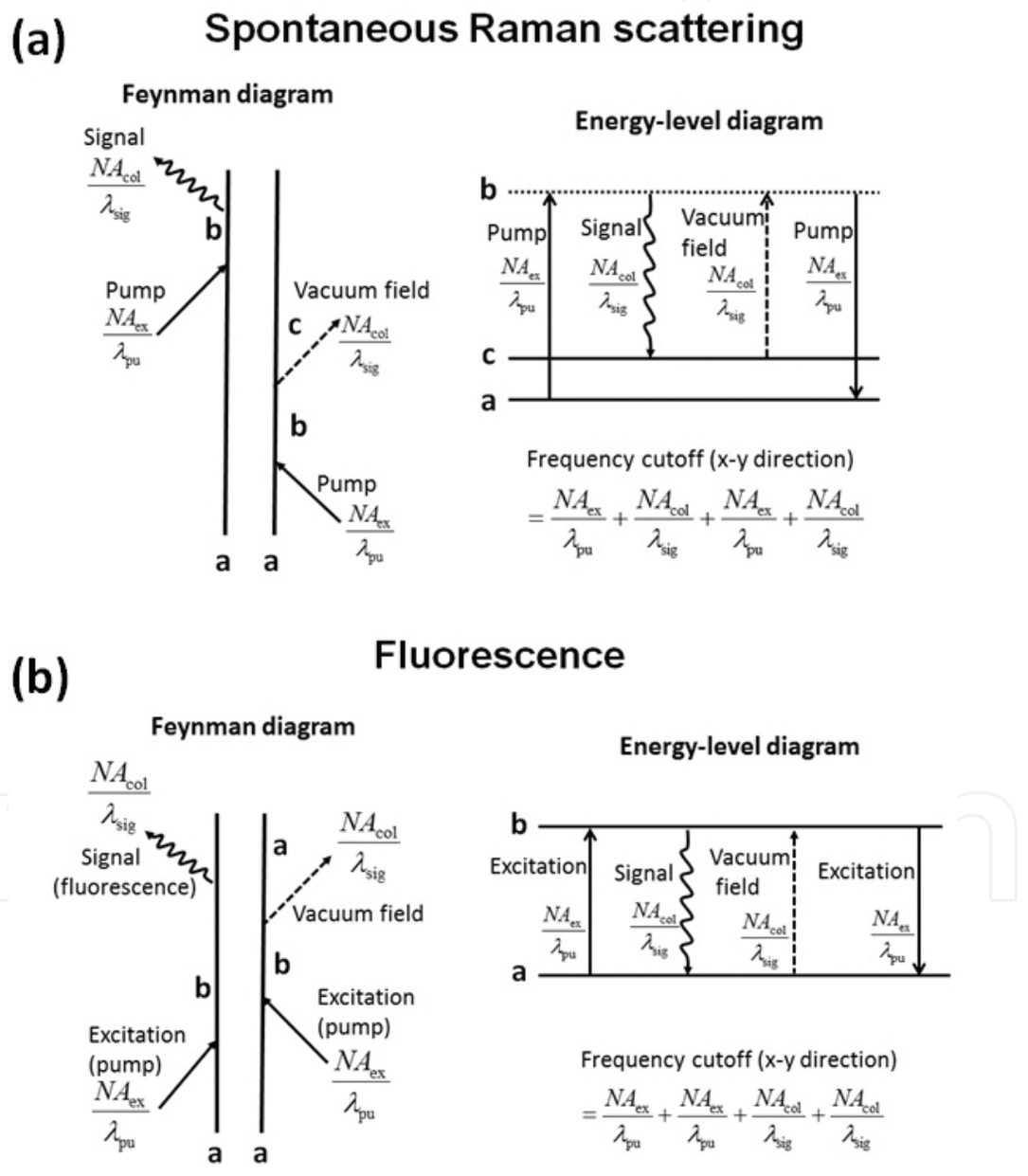

Figure 9. Double-sided Feynman diagram and energy-level diagram for (a) spontaneous Raman scattering and (b) fluorescence.

http://dx.doi.org/ 10.5772/63494

To discuss the maximum value of the frequency cutoff, we concentrate on confocal microscopy. Substituting $\delta(x_a)\ \delta(y_a)$ into $a(x_a, y_a)$, we obtain the image-forming formula of confocal Raman microscopy as follows:

$$I_{\mathrm{Ra}}^{c}(x',y',z') = \iiint \mathrm{Im}\{-2\chi_{\mathrm{SRG}}^{(3)}(x+x',y+y',z+z')\} \mid E_p(x,y,z)\mid^2 \mid E_{\mathrm{col}}(-x,-y,-z)\mid^2 dxdydz. \tag{30}$$

Another example of an incoherent optical process is fluorescence. For the image-forming formula of confocal fluorescence microscopy, we only replace $\chi_{\mathrm{SRG}}^{(3)}(x, y, z)$ with $\chi_{\mathrm{SE}}^{(3)}(x, y, z)$, namely,

$$I_{\mathrm{flu}}^{c}(x',y',z') = \iiint \mathrm{Im}\{-2\chi_{\mathrm{SE}}^{(3)}(x+x',y+y',z+z')\} \mid E_p(x,y,z)\mid^2 \mid E_{\mathrm{col}}(-x,-y,-z)\mid^2 dxdydz. \tag{31}$$

Although the ASF of spontaneous Raman scattering and that of fluorescence microscopy are represented by the same notation, it is notable that the double-sided Feynman diagrams or energy-level diagrams for these two processes are different, as described in **Figure 9**.

3. Optical resolution limit

In Section 2, we covered all types of laser microscopy, which include (i) coherent microscopy with the signal wavelength different from the excitation wavelength, (ii) coherent microscopy with the signal wavelength identical with the excitation wavelength, and (iii) incoherent microscopy.

In type (i), the signal can be measured by blocking the excitation beam with the filter. In type (ii), the signal can be extracted by lock-in detection, except linear microscopy that utilizes a $\chi^{(1)}$-derived optical process. Type (ii) has the local oscillator interfering with the signal, while type (i) does not have the local oscillator. Type (iii) is described in the same fashion as type (ii). Interestingly, in type (iii), the vacuum field plays a role as the local oscillator.

In this section, we form the framework that can discuss the resolution limit for all types of laser microscopy by using double-sided Feynman diagrams and energy-level diagrams. It is well known that the image of the object is formed in three dimensions by laser microscopy with a finite optical resolution, determined by the NA of the excitation and signal-collection systems and the wavelengths of the excitation beams and signal. In addition, we show that the type of optical process occurring in the sample also influences the optical resolution. In our model, the distribution of the linear or nonlinear susceptibility $\chi^{(i)}(x, y, z)$ corresponds to the object we would like to visualize. While the double-sided Feynman diagram was developed to calculate the quantity of susceptibility, which depends on the type of optical process involved, we provide the calculation method for the optical resolution of laser microscopy, which is also linked to the double-sided Feynman diagram.

Our model includes coherent microscopy and incoherent microscopy. Regardless of the coherence, we deal with all types of laser microscopy in the identical framework. In coherent microscopy, the coherent interaction between the excitation laser beam and the molecule occurs, and the corresponding susceptibility distribution is visualized in the image. In incoherent microscopy, an incoherent optical process, which is caused by the excitation beam and the vacuum field lying in the object space, takes place, and the image of the corresponding susceptibility distribution is created. Incoherent microscopy exhibits the incoherent property inherited from the vacuum field. For incoherent microscopy, the equation is formulated by partially using quantum optical notation.

In incoherent microscopy, the definition of the optical resolution becomes straightforward by utilizing the optical transfer function (OTF), while in coherent microscopy, because the OTF does not exist, some definitions are conceivable. In this section, for both coherent microscopy and incoherent microscopy, we define the resolution limit as the largest grating vector that can be resolved, when the three-dimensional grating of the susceptibility is observed as the object. By using our theoretical framework described below, the frequency cutoffs (resolution limits) of coherent microscopy and incoherent microscopy can be compared.

3.1. Diagram technique

We introduce the double-sided Feynman diagram to discuss the frequency cutoff. Originally, this diagram was developed to count and categorize the optical processes and calculate the nonlinear susceptibility of each one. Here we connect the diagram to the frequency cutoffs of linear, nonlinear, coherent, and incoherent microscopy. The diagram can deal with all optical processes, including incoherent processes, such as fluorescence and spontaneous Raman scattering. In coherent microscopy, the resolution limits of confocal and nonconfocal systems are identical, while in incoherent microscopy, the confocal system exhibits the better optical resolution than the nonconfocal system. Note that in coherent microscopy, the images of the confocal and nonconfocal systems indicate the different contrasts. To discuss the theoretical maximum value of the frequency cutoff, we deal with the confocal system for both coherent microscopy and incoherent microscopy. We consider the ASF and its Fourier transform: CTF. For incoherent microscopy, although the point spread function (PSF) is ordinarily used instead of ASF, in this section we refer to PSF for incoherent microscopy as ASF, to integrate coherent microscopy and incoherent microscopy into the identical framework.

The essential part of the image-forming formula for all types of microscopy can be written as

$$I(x',y',z') = \iiint O^{(i)}(x+x',y+y',z+z')\mathrm{ASF}(x,y,z)dxdydz, \tag{32}$$

or the square of its modulus. Here $O^{(i)}$ (x, y, z) corresponds to the object originating from $\chi^{(i)}$ (x, y, z). To discuss the largest grating vector that can be resolved, we consider 3-D grating as the object. In this case, we can just concentrate on Eq. (32), because the resolution limit does not change regardless of whether Eq. (32) is squared or not. The Fourier transform of Eq. (32) is given by

http://dx.doi.org/ 10.5772/63494

$$\tilde{I}(f_x, f_y, f_z) = \tilde{O}^{(i)}(f_x, f_y, f_z) CTF(f_x, f_y, f_z), \tag{33}$$

where $\tilde{A}$ means the Fourier transform of A and $(f_x, f_y, f_z)=(k_x/2\pi, k_y/2\pi, k_z/2\pi)$, which corresponds to the grating vector. For convenience, we use the definition that the Fourier transform of $\{\mathrm{ASF}(x, y, z)\}^*$ is $\{\mathrm{CTF}(f_x, f_y, f_z)\}^*$. The CTF expresses the existence range of the grating vector that can be resolved. In transmission linear confocal microscopy, for example, $\mathrm{ASF}(x, y, z)$ is equal to $E_{ex}(x, y, z)E_{col}(-x, -y, -z)$, and Fourier transforming it leads to $\mathrm{CTF}(f_x, f_y, f_z)=U_{\mathrm{ex}}(-f_x, -f_y, -f_z) \otimes U_{\mathrm{col}}(f_x, f_y, f_z)$, where $U_{\mathrm{col}}(f_x, f_y, f_z)$ and $U_{\mathrm{ex}}(f_x, f_y, f_z)$ stand for the Fourier transforms of $E_{\mathrm{col}}(x, y, z)$ and $E_{\mathrm{ex}}(x, y, z)$, respectively. Considering the Ewald sphere helps in understanding the CTF. The Ewald sphere in this case has the same radii as $U_{\mathrm{col}}(f_x, f_y, f_z)$ and $U_{\mathrm{ex}}(f_x, f_y, f_z)$, which are partial spheres (3-D pupil functions) as mentioned above. The phase-matching condition (momentum conservation law), $\boldsymbol{k}_{\mathrm{sig}} = \boldsymbol{k}_{\mathrm{ex}} + \boldsymbol{K}$, is satisfied with the Ewald sphere, where $\boldsymbol{k}_{\mathrm{ex}}$ and $\boldsymbol{k}_{\mathrm{sig}}$ are the wavenumber vectors of the excitation light and the signal, respectively, and $\boldsymbol{K}$ is the grating vector in the sample. Unless the phase-matching condition is satisfied as shown in **Figure 10**, the signal cannot be generated. Consequently, the resolvable grating vector is restricted to the range determined by the CTF.

In analogy with the above formulation, also for any laser microscopy, the phase-matching condition is taken into account. Since the focused excitation beam is composed of numerous plane waves, all combinations of the excitation plane wave need to be considered. In coherent microscopy, only if the sum of the wavenumber vector of each excitation plane wave and the grating vector of the susceptibility is equal to the wavenumber vector of the signal that can be collected by the signal-collection system, the signal can be generated and detected by the signal-collection system. The phase-matching condition (e.g., $\boldsymbol{k}_{\mathrm{sig}} = \boldsymbol{k}_{\mathrm{ex1}} - \boldsymbol{k}_{\mathrm{ex2}} + \cdots + \boldsymbol{k}_{\mathrm{exn}} + \boldsymbol{K}$) can be connected to the double-sided Feynman diagram and energy-level diagram as follows:

1. For the right-pointing arrow in the Feynman diagram or the up-pointing arrow in the energy-level diagram, the wavenumber vector of the excitation light corresponds to $+\boldsymbol{k}_{\mathrm{ex}}$.
2. For the left-pointing arrow in the Feynman diagram or the down-pointing arrow in the energy-level diagram, the wavenumber vector of the excitation light corresponds to $-\boldsymbol{k}_{\mathrm{ex}}$.

   The focused excitation beams and the signal contain many plane waves whose wavenumber vectors lie on the 3-D pupil functions. The ASF (e.g., $E_{\mathrm{ex1}}(\boldsymbol{x})E^*_{\mathrm{ex2}}(\boldsymbol{x}) \cdots E_{\mathrm{exn}}(\boldsymbol{x})E_{\mathrm{col}}(-\boldsymbol{x})$) obeys the following rule.

3. For the right-pointing arrow in the Feynman diagram or the up-pointing arrow in the energy-level diagram, the electric field distribution formed by the excitation beam corresponds to $E_{\mathrm{ex}}(\boldsymbol{x})$.
4. For the left-pointing arrow in the Feynman diagram or the down-pointing arrow in the energy-level diagram, the electric field distribution formed by the excitation beam corresponds to $E^*_{\mathrm{ex}}(\boldsymbol{x})$.

5. For the wavy-line arrow, the electric field distribution $E_{\mathrm{col}}(-\boldsymbol{x})$ formed by the signal through the signal-collection system is applied.

   The CTF (e.g., $U_{\mathrm{ex1}}(-\boldsymbol{f}) \otimes U^{*}_{\mathrm{ex2}}(\boldsymbol{f}) \otimes \cdots \otimes U_{\mathrm{exn}}(-\boldsymbol{f}) \otimes U_{\mathrm{col}}(\boldsymbol{f})$) satisfies the following rule.

6. For the right-pointing arrow in the Feynman diagram or the up-pointing arrow in the energy-level diagram, the 3-D pupil function for the excitation beam corresponds to $U_{\mathrm{ex}}(-\boldsymbol{f})$.

7. For the left-pointing arrow in the Feynman diagram or the down-pointing arrow in the energy-level diagram, the 3-D pupil function for the excitation beam corresponds to $U^{*}_{\mathrm{ex2}}(\boldsymbol{f})$.

8. For the wavy-line arrow, the 3-D pupil function for the signal $U_{\mathrm{col}}(\boldsymbol{f})$ is applied.

   As an example of coherent microscopy, **Figure 10** describes the relation between the CTF and the phase-matching condition represented by the 3-D pupil function. The figure shows the case of linear confocal microscopy, but in the case of nonlinear coherent microscopy, the nonzero region of the CTF becomes larger and the missing cone in the z direction disappears. While the CTF can be calculated by the above rule, the frequency cutoff in the x-y direction can be evaluated more easily with the following rule.

9. Each arrow for the excitation is connected to $\mathrm{NA}_{\mathrm{ex}}/\lambda'$, where λ' is the wavelength of the corresponding beam, such as pump or Stokes.

10. The arrow for the signal is connected to $\mathrm{NA}_{\mathrm{col}}/\lambda_{\mathrm{sig}}$.

11. The maximum possible value of the frequency cutoff in the x-y direction is given by the sum of all the above-mentioned values: $\Sigma\{\mathrm{NA}/\lambda\}$.

    In incoherent microscopy, the vacuum field, which contains the virtual photons with the wavenumber vectors in all directions, plays a role as one of the excitation light. The vacuum field is described by the right-pointing dashed arrow in the double-sided Feynman diagram and up-pointing dashed arrow in the energy-level diagram. The vacuum field has its own rule as follows.

12. The wavenumber vector for the vacuum field corresponds to $+\boldsymbol{k}_{\mathrm{vac}}$.

13. For the ASF, the electric field distribution for the vacuum field corresponds to $E^{*}_{\mathrm{col}}(-\boldsymbol{x})$.

14. For the CTF, the 3-D pupil function for the vacuum field corresponds to $U^{*}_{\mathrm{col}}(-\boldsymbol{f})$.

15. For the frequency cutoff in the x-y direction, the corresponding value for the vacuum field is $\mathrm{NA}_{\mathrm{col}}/\lambda_{\mathrm{sig}}$, which is the same value as that of the signal.

Note that in incoherent microscopy, the CTF is referred to as the OTF and the ASF becomes the PSF. The vacuum field around the sample includes the Fourier components that have the wavenumber vectors also on the side opposite to the excitation beam. As a result, for reflection microscopy, $|E_{\mathrm{col}}(x_{\mathrm{a}}-x,\ y_{\mathrm{a}}-y,\ z_{\mathrm{a}}-z)|^2$ in Eq. (29) can be replaced by $|E'_{\mathrm{col}}(x_{\mathrm{a}}-x,\ y_{\mathrm{a}}-y,\ z_{\mathrm{a}}-z)|^2$, but both become the same function if the NAs are identical. Thus,

http://dx.doi.org/ 10.5772/63494

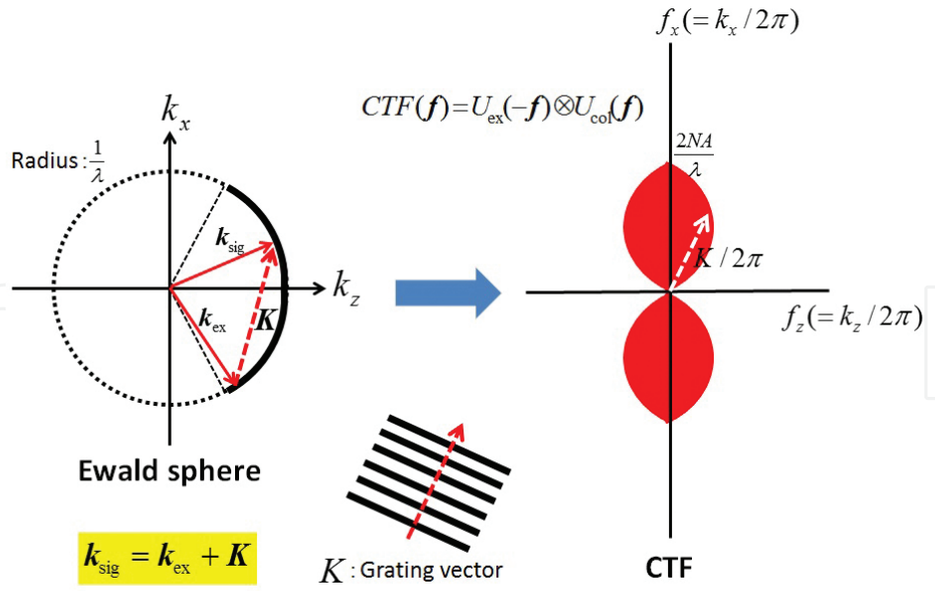

Figure 10. The relation between the phase-matching condition and the CTF for transmission linear confocal microscopy.

unlike in coherent microscopy, it turns out that the OTF of transmission microscopy is identical with that of reflection microscopy in incoherent microscopy. As an example of incoherent microscopy, we take the transmission fluorescence confocal microscopy shown in **Figure 11**, where the relation between the CTF and the phase-matching condition is described with the 3-D pupil function.

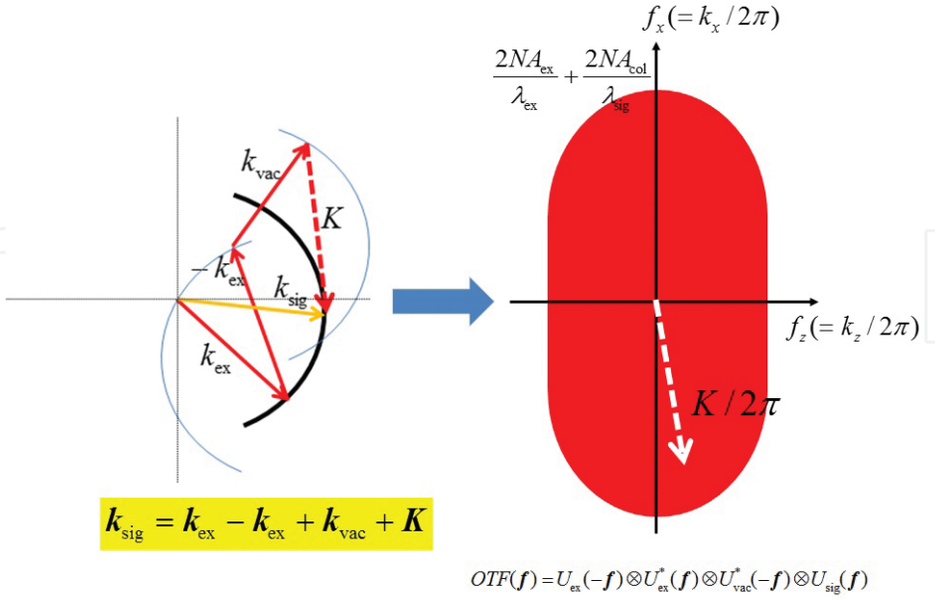

Figure 11. The relation between the phase-matching condition and the CTF for the transmission fluorescence confocal microscopy. Note that $U_{col}^{*}(-f)=U_{vac}^{*}(-f)$ and $U_{col}(f)=U_{sig}(f)$

4. Discussion

As stated above, the maximum possible resolution limit is determined by the kind of optical process in force. For illustration, **Figure 12** shows the calculation results of the CTF for CARS, stimulated Raman loss (SRL), SRG, and third-order harmonic generation (THG) microscopy [4]. For reference, the double-sided Feynman diagram and the energy-level diagram describing SRL and THG are shown in **Figure 13**. SRL microscopy and SRG microscopy have the same resolution limit, while CARS microscopy shows better optical resolution than the two former techniques. The CTF of THG microscopy exhibits peculiar properties in which the value of the origin in the spatial frequency domain is zero.

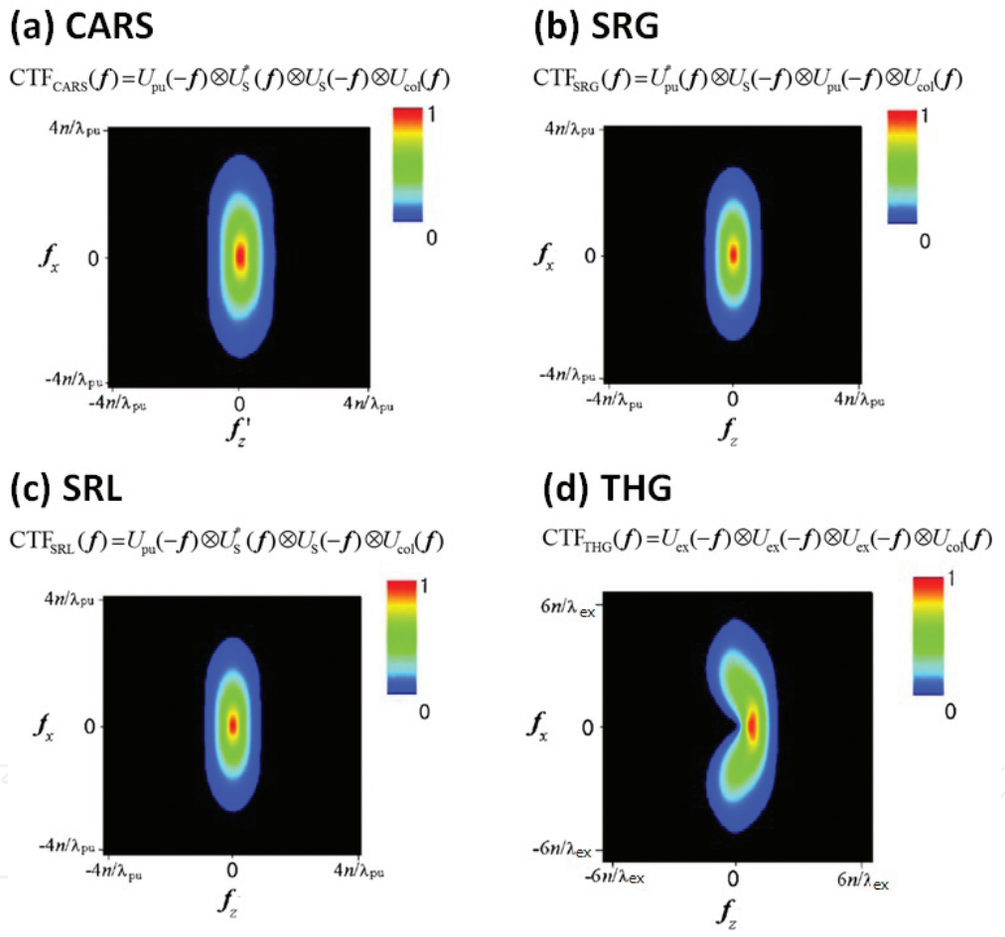

Figure 12. Calculation samples of the CTF for (a) CARS, (b) SRG, (c) SRL, and (d) THG microscopy.

From our theory, some interesting results are also obtained. In reflection coherent microscopy, the uniform region of the susceptibility disappears in the image, as does the interface whose normal is perpendicular to the optical axis. As an example to see the difference between reflection and transmission microscopy, the CTF of transmission and reflection CARS microscopy are shown in **Figure 14** [13]. In transmission THG microscopy, the dot and interface of the susceptibility are emphasized in the image and the uniform region vanishes. In reflection

CARS microscopy and transmission THG microscopy, the grating of susceptibility cannot be resolved, but by assembling the interference microscopy where the signal interferes with the local oscillator generated separately, the grating becomes resolved and then the optical resolution can be defined.

In incoherent microscopy such as fluorescence and spontaneous Raman scattering microscopy, the vacuum field as well as the excitation beam are involved in the optical process and contribute to the increase in the frequency cutoff. It is noteworthy about incoherent microscopy that the OTFs of the transmission and reflection microscopy becomes equal. On the other hand, in coherent microscopy such as SHG, THG, CARS, SRG, and SRL microscopy, the CTFs of transmission and reflection microscopy differ from each other.

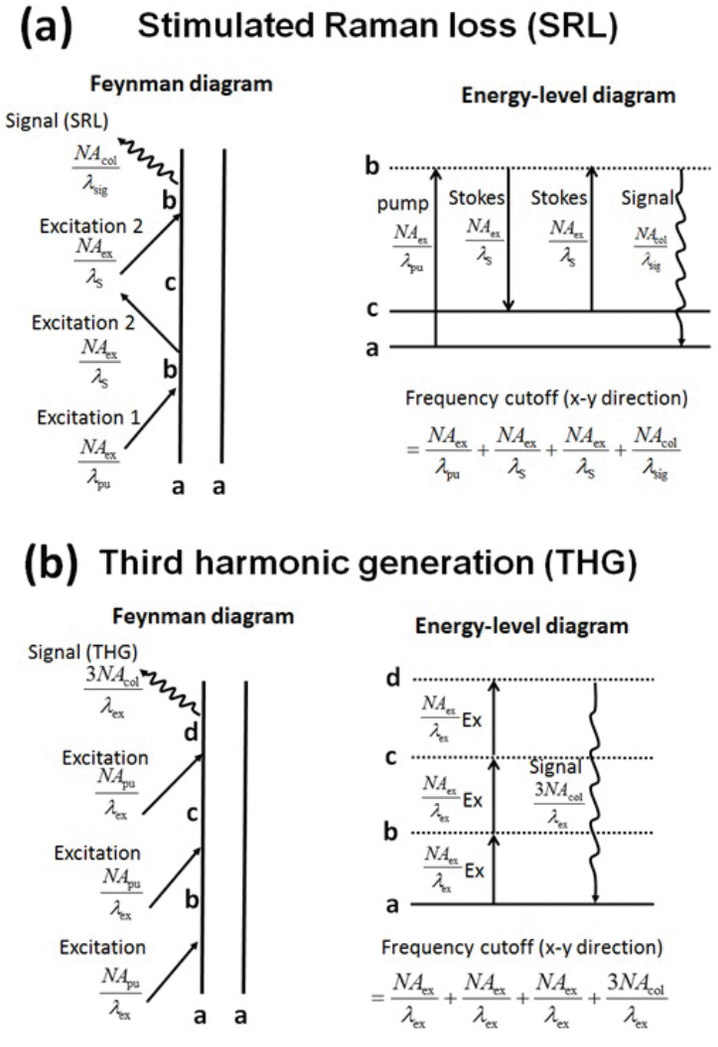

Figure 13. Double-sided Feynman diagram and energy-level diagram for (a) SRL and (b) THG.

Without restricting laser scanning (stage-scanning) microscopy, we can conjecture the following theorem of the resolution limit for all types of microscopy, which visualize $\chi^{(i)}(x, y, z)$ through a variety of optical processes.

4.1. Theorem

- If there is no a priori information on the object (sample), the resolution limit (the maximum value of frequency cutoff) is determined by the diagram describing the optical process. As long as the optical process described by a certain diagram is used to visualize $\chi^{(i)}(x, y, z)$, the resolution limit calculated from the diagram cannot be surpassed regardless of how well the optical apparatus is devised.

The typical exception to the above theorem is localization microscopy, such as photo-activated localization microscopy (PALM) [14] and stochastic optical reconstruction microscopy (STORM) [15], which have a priori information on the object (isolated single-point object). Any microscopy application, including SIM and stimulated emission depletion (STED) microscopy [16], that does not have a priori information on the object should follow this theorem.

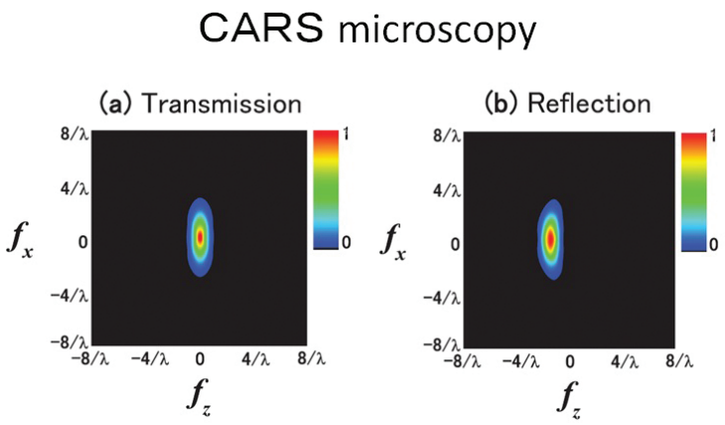

Figure 14. The CTF of transmission and reflection CARS microscopy.

5. Conclusions

We have constructed a theoretical framework to deal with the image formation of all kinds of microscopy by using the double-sided Feynman diagrams and energy-level diagrams describing optical processes. We discovered some rules to evaluate the resolution limit by using these diagrams. Our diagram technique can overview laser microscopy with any optical processes regardless of coherence or linearity. In our framework, the susceptibility distribution is visualized in the image, which blurs based on the optical resolution of each type of microscopy calculated from the diagram technique. Interestingly, in microscopy with an incoherent process, the vacuum field plays a role as part of the excitation light and contributes to the improvement of the optical resolution. In nonconfocal systems, which is commonly used to acquire a high-intensity signal particularly in nonlinear microscopy, the resolution limit of incoherent microscopy is determined by the excitation system only, whereas that of coherent microscopy is determined by both the excitation and signal-collection systems. In SRS microscopy, the transmission type mainly observes the imaginary part of the nonlinear susceptibility, while the reflection type can detect the real part.

http://dx.doi.org/ 10.5772/63494

Author details

Naoki Fukutake

Address all correspondence to: Naoki.Fukutake@nikon.com

Nikon Corporation, Yokohama, Japan

References

[1] M. Born and E. Wolf. Principles of Optics. 5th ed. Pergamon Press (Oxford); 1974.

[2] M. G. Gustafsson. Surpassing the lateral resolution limit by a factor of two using structured illumination microscopy. J. Microsc. 2000;198:82–87.

[3] M. Gu. Principles of three dimensional imaging in confocal microscopes. World Scientific (Singapore); 1996.

[4] N. Fukutake. Comparison of image-formation properties of coherent nonlinear microscopy by means of double-sided Feynman diagrams. J. Opt. Soc. Am. B. 2013;30:2665–2675.

[5] W. Denk, J. H. Strickler, and W. W. Webb. Two-photon laser scanning fluorescence microscopy. Science. 1990;248:73–76.

[6] W. R. Zipfel, R. M. Williams, and W. W. Webb. Nonlinear magic: multiphoton microscopy in the biosciences. Nat. Biotechnol. 2003;21:1369–1377.

[7] I. Freund and M. Deutsch. Second-harmonic microscopy of biological tissue. Opt. Lett. 1986;11:94–96.

[8] Y. Barad, H. Eisenberg, M. Horowitz, and Y. Silberberg. Nonlinear scanning laser microscopy by third-harmonic generation. Appl. Phys. Lett. 1997;70:922–924.

[9] M. D. Duncan, J. Reintjes, and T. J. Manuccia. Scanning coherent anti-Stokes Raman microscope. Opt. Lett. 1982;7:350–352.

[10] A. Zumbusch, G. R. Holtom, and X. S. Xie. Vibrational microscopy using coherent anti-Stokes Raman scattering. Phys. Rev. Lett. 1999;82:4142–4145.

[11] W. Freudiger, W. Min, B. G. Saar, S. Lu, G. R. Holtom, C. He, J. C. Tsai, J. X. Kang, and X. S. Xie. Label-free biomedical imaging with high sensitivity by stimulated Raman scattering microscopy. Science. 2008;322:1857–1861.

[12] S. Kawata, R. Arimoto, and O. Nakamura. Three-dimensional optical-transfer-function analysis for a laser-scan fluorescence microscope with an extended detector. J. Opt. Soc. Am. A. 1991;8:171–175.

[13] N. Fukutake. Coherent transfer function of Fourier transform spectral interferometric coherent anti-Stokes Raman scattering microscopy. J. Opt. Soc. Am. A. 2011;28:1689–1694.

[14] E. Betzig, G. H. Patterson, R. Sougrat, O. W. Lindwasser, S. Olenych, J. S. Bonifacino, M. W. Davidson, J. Lippincott-Schwartz, and H. F. Hess. Imaging intracellular fluorescent proteins at nanometer resolution. Science. 2006;313:1642–1645.

[15] M. J. Rust, M. Bates, and X. Zhuang. Sub-diffraction-limit imaging by stochastic optical reconstruction microscopy (STORM). Nature Methods. 2006;3:793–796.

[16] S. W. Hell and J. Wichmann. Breaking the diffraction resolution limit by stimulated emission: stimulated-emission-depletion fluorescence microscopy. Opt. Lett. 1994;19:780–782.